Front. Energy 2023, 17(4): 463–477
https://doi.org/10.1007/s11708-023-0860-1

REVIEW ARTICLE

Yuan LIN, Jiazheng HAO, Kaiming QIAO, Yihong GAO, Fengxia HU, Jing WANG, Tongyun ZHAO, Baogen SHEN

Phase transition regulation and caloric effect

Abstract Solid state refrigeration based on caloric effect is regarded as a potential candidate for replacing vapor-compression refrigeration. Numerous methods have been proposed to optimize the refrigeration properties of caloric materials, of which single field tuning as a relatively simple way has been systemically studied. However, single field tuning with few tunable parameters usually obtains an excellent performance in one specific aspect at the cost of worsening the performance in other aspects, like attaining a large caloric effect with narrowing the transition temperature range and introducing hysteresis. Because of the shortcomings of the caloric effect driven by a single field, multifield tuning on multicaloric materials that have a coupling between different ferro-orders came into view. This review mainly focuses on recent studies that apply this method to improve the cooling performance of materials, consisting of enlarging caloric effects, reducing hysteresis losses, adjusting transition temperatures, and widening transition temperature spans, which indicate that further progress can be made in the application of this method. Furthermore, research on the sign of lattice and spin contributions to the magnetocaloric effect found new phonon evolution mechanisms, calling for more attention on multicaloric effects. Other progress including improving cyclability of FeRh alloys by introducing second phases and realizing a large reversible barocaloric effect by hybridizing carbon chains and inorganic groups is described in brief.

Keywords phase transition regulation, caloric effect, solid state refrigeration

Received Oct. 18, 2022; accepted Dec. 18, 2022; online Feb. 28, 2023

Yuan LIN, Yihong GAO, Jing WANG
Beijing National Laboratory for Condensed Matter Physics, Institute of Physics, Chinese Academy of Sciences, Beijing 100190, China; School of Physical Sciences, University of Chinese Academy of Sciences, Beijing 101408, China

Jiazheng HAO
Spallation Neutron Source Science Center, Dongguan 523803, China; Institute of High Energy Physics, Chinese Academy of Sciences, Beijing 100049, China

Kaiming QIAO
School of Materials Science and Engineering, University of Science and Technology Beijing, Beijing 100083, China

Fengxia HU (✉)
Beijing National Laboratory for Condensed Matter Physics, Institute of Physics, Chinese Academy of Sciences, Beijing 100190, China; School of Physical Sciences, University of Chinese Academy of Sciences, Beijing 101408, China; Songshan Lake Materials Laboratory, Dongguan 523808, China
E-mail: fxhu@iphy.ac.cn

Tongyun ZHAO
Beijing National Laboratory for Condensed Matter Physics, Institute of Physics, Chinese Academy of Sciences, Beijing 100190, China; Ganjiang Innovation Academy, Chinese Academy of Sciences, Ganzhou 341000, China

Baogen SHEN
Beijing National Laboratory for Condensed Matter Physics, Institute of Physics, Chinese Academy of Sciences, Beijing 100190, China; School of Physical Sciences, University of Chinese Academy of Sciences, Beijing 101408, China; Ningbo Institute of Materials Technology and Engineering, Chinese Academy of Sciences, Ningbo 315201, China; Ganjiang Innovation Academy, Chinese Academy of Sciences, Ganzhou 341000, China

Special Column: Caloric Refrigeration for Zero-carbon Active Cooling and Heating

1 Introduction

Nowadays, relying on the advantage of high specific cooling power (SCP), vapor compression refrigeration is used in most commercial cooling machines like air-conditioners. However, with the use of chemical refrigerants and low cooling efficiency causing large carbon dioxide emissions, this technique worsens the greenhouse effect. The fast development of the economy and the explosion of population bring up urgent needs for more environmentally friendly and more efficient refrigeration prototypes.

Fortunately, the potential solid-state refrigeration technique based on caloric effects including the magnetocaloric effects [1–10], the electrocaloric effects [11–17], the elastocaloric effects [18–21], and the barocaloric [22–33] effects induced by magnet fields,

electric fields, uniaxial stresses, and hydrostatic pressures respectively, seems to be the redeemer. Caloric effects are defined as isothermal entropy changes or adiabatic temperature changes during the phase transition process triggered by an external field. The chemical refrigerant independence, the high working efficiency, the possibility of minimization, and the noiseless working cycle make caloric effects promising candidates for alternating vapor compression refrigeration. A great deal of effort has been devoted to this field to pursue excellent performances: large entropy changes, low hysteresis losses, wide transition temperature spans, and a good cyclability.

Up to the present, most studies have been concentrated on the caloric effect driven by a single field, leading to the competition of pursuing caloric materials with high isothermal entropy changes. Many first-order materials featuring magnetostructural/magnetoelastic transition have been discovered showing large entropy changes, such as $Gd_5Si_2Ge_2$ [34,35], FeRh [36,37], and $La(Fe,Si)_{13}$ [38], but it is at the cost of sacrificing low hysteresis losses, wide transition temperature spans, and good cyclability [39–48]. To make the best of both worlds, an extra tool, multifield tuning heaves in sight [49]. Correspondingly, the multiferroic material is the one possessing more than one ferroic order, thus replying to different fields. One ferroic order can be changed by various fields if it is strongly coupled to another ferroic order. Consequently, caloric effects could be influenced by each other because of the couple between ferroic orders. Therefore, it is feasible to realize unprecedented performance based on this principle.

In this review, first, the sign of lattice and spin contribution in the magnetostructural transition will be discussed. Then, applying multifield tuning, the improvement to the magnitude of caloric effects, the decrease of hysteresis, the wideness of transition temperature spans, and the coupled caloric effect will be demonstrated in order. Finally, the promotion of cyclability and large reversible barocaloric effects will be shown.

2 Multifield tuning

2.1 Sign of lattice and spin contributions during a magnetostructural/magnetoelastic transition

For giant magnetocaloric materials, along with the magnetic phase transition, the lattice parameter and/or the crystal symmetry also discontinuously transform, i.e., a first-order transition. For a transition from the ferromagnetic (FM) to the paramagnetic (PM) phase, if the lattice expands, it is well known that both the lattice and the spin entropy increase like $Gd_5(Si_xGe_{1-x})_4$ [34,50] with a lattice expansion $\Delta V/V$ about +(0.4–1.0)%. On the contrary, arousing controversy, it is ambiguous whether the sign of entropy changes is the same or not for the negative lattice expansion, for instance, $La(Fe,Si)_{13}$-based compounds with a lattice contraction $\Delta V/V$ about –(1.2–1.6)% [3,38,51], MnAs-based with $\Delta V/V$ about –(1.1–2.1)% [42,52], and MnCoGe/MnNiGe-based with $\Delta V/V$ about –(2.8–3.9)% [53–56] during the magnetostructural or magnetoelastic transition. It is acknowledged that the spin entropy in the PM phase is larger than that in the FM phase and usually the phase with a larger lattice parameter should possess a larger lattice entropy. Therefore, the magnetic field drives the transition from the PM phase to the FM phase, enlarging the lattice entropy and lowering the spin entropy. For instance, the investigation on MnAs conducted by density functional theory (DFT) indicates that the sign of the spin entropy change should be different from that of the lattice [57], but no experiment has been conducted to prove it up to the present. Jia et al. once reported that the smaller positive phonon entropy change was covered by the larger negative spin entropy change, thus leading to a totally negative entropy change in $La(Fe,Si)_{13}$-based magnetic materials [58]. But, surprisingly, employing nuclear resonant inelastic X-ray scattering (NRIXS), the research done by Landers et al. showed that the magnitude of the Fe-partial lattice entropy change of about 6.9 (± 2.6) J/(kg·K) was about 49% of the total entropy change 14.2 J/(kg·K) obtained for $LaFe_{11.6}Si_{1.4}$ at a 0–1 T magnetic field using Maxwell relation, and the sign was the same as the total entropy change [59,60]. Luckily, since the separation and the couple of the magnetic and structural transition of MnCoGe and MnNiGe alloys can be controlled by pressure or doping, studies have confirmed that the sign of lattice and spin contribution is the same [55,56,61].

In the 1970s, Johnson [55], and Anzai & Ozawa [56] respectively investigated transitions of MnCoGe and MnNiGe, and found that there was a separate magnetic transition from the FM/antiferromagnetic (AFM) phase to the PM phase and a structural transition with a lattice contraction $\Delta V/V$ about –(1.6–3.9)% upon heating (Fig. 1(a)). By utilizing differential scanning calorimetry (DSC) or differential thermal analysis (DTA) to monitor the heat flow during either the heating or the cooling process, the direction of different peaks is demonstrated to be the same (Figs. 1(b), 1(d)). Moreover, Anzai and Ozawa [56] revealed that the two transitions evolved into one transition with pressure increasing, further proving that the lattice entropy decreased in the magnetostructural transition upon cooling with lattice expanding (Fig. 1(d)). Substituting Ge with Al, Bao et al. [61] studied the properties of the magnetostructural transition in $MnCoGe_{1-x}Al_x$. Since Al stabilizes the hexagonal structural phase and shifts the structural transition to lower temperatures, it can control the relative position of the two peaks. For x = 0.01, 0.02, it realizes a magnetostructural transition while for $x \geqslant 0.03$, it

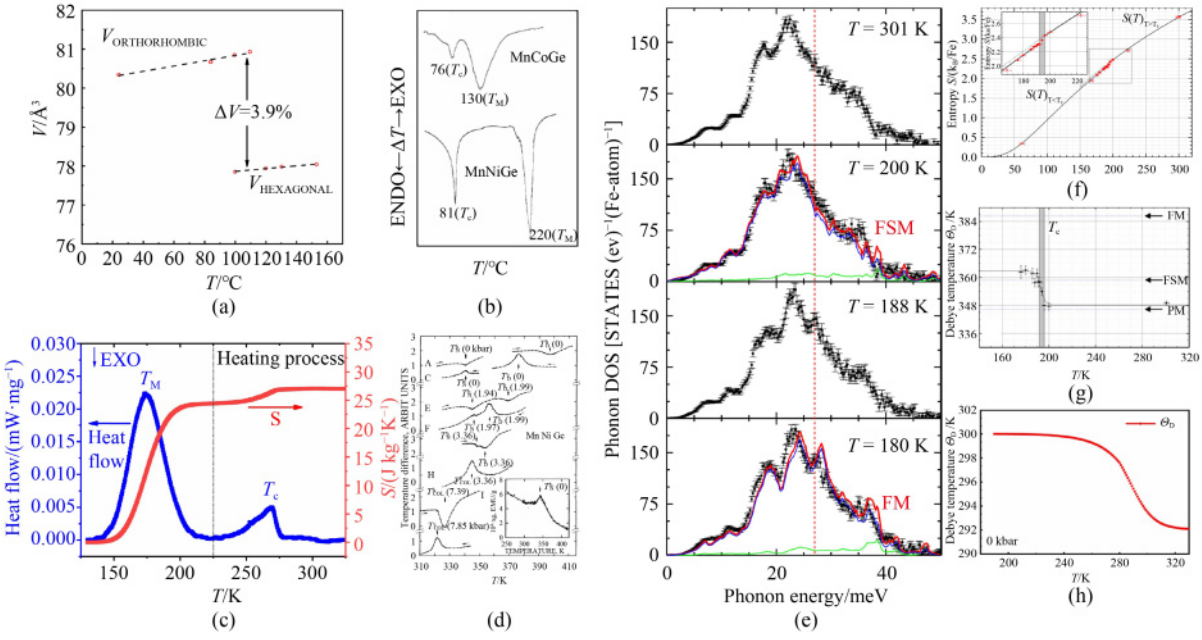

Fig. 1 Clarification of the sign of the lattice and spin contribution to the entropy change.

(a) Change of the lattice volume of MnCoGe alloys during phase transition [55] (adapted with permission from Ref. [55], Copyright 1975, American Chemical Society); (b) heat flux peaks recorded by DSC for MnCoGe and MnNiGe alloys [55] (adapted with permission from Ref. [55], Copyright 1975, American Chemical Society); (c) heat flux upon heating recorded by DSC and the entropy calculated by the heat flux as a function of temperature for $MnCoGe_{0.97}Al_{0.03}$ alloys [65] (reprinted with permission from Ref. [65], Copyright 2020, Elsevier); (d) heat flux curves at different pressures for MnNiGe alloys recorded by DTA [56] (reprinted with permission from Ref. [56], Copyright 1978, American Physical Society); (e) Fe-partial VDOS of $LaFe_{11.6}Si_{1.4}$ powder with a transition temperature of about 192 K obtained from ^{57}Fe (accounting for 10% of the total Fe) NRIXS measured at different temperatures in the magnetic field of 0.7 T [60] (reprinted with permission from Ref. [60], Copyright 2018, American Physical Society); (f) vibrational entropy of Fe sublattice computed by Fe-partial VODS of $LaFe_{11.6}Si_{1.4}$ powder [60] (reprinted with permission from Ref. [60], Copyright 2018, American Physical Society); (g) Debye temperature calculated from Lamb-Mössbauer factor f_{LM} based on Fe-partial VDOS data for $LaFe_{11.6}Si_{1.4}$ compounds [60] (reprinted with permission from Ref. [60], Copyright 2018, American Physical Society); (h) variation of Debye temperature with the change of temperature for $La(Fe_{0.92}Co_{0.08})_{11.9}Si_{1.1}$ compounds computed by Debye approximation without introducing pressure [64] (reprinted with permission from Ref. [64], Copyright 2020, American Chemical Society).

separates again. Upon heating, the heat flow measurement shows that the lattice entropy increases with the lattice contracting for $x = 0.03$, verifying that the sign of lattice entropy changes does nothing with the relative position of the two peaks. Therefore, the sameness of the sign of spin and lattice entropy changes is further proved (Fig. 1(c)).

The direct experimental proof was shown by Landers et al. to testify that the sign of spin and lattice entropy changes of $La(Fe,Si)_{13}$ was the same [59,60]. The vibration density of states (VDOS) in $LaFe_{11.6}Si_{1.4}$ around the phase transition temperature was measured, indicating that a phonon peak around 27 meV disappeared upon heating which meant that the phonon softened, leading to an entropy increase (Fig. 1e). Applying the thermodynamic relation

$$S_{\mathrm{Latt}}(T) = 3k_{\mathrm{B}}\int_0^{\infty} g(E)\left[\frac{\beta E(e^{\beta E}+1)}{2(e^{\beta E}-1)} - \ln\left(e^{\frac{\beta E}{2}} - e^{-\frac{\beta E}{2}}\right)\right]\mathrm{d}E, \tag{1}$$

where S_{Latt} is the lattice entropy, T is temperature, k_{B} is Boltzmann constant, $g(E)$ is the density of states, E is the energy of state, and β equals $1/(k_{\mathrm{B}}T)$. The results calculated by VDOS data expressed that the increase of Fe-partial entropy was 6.9(± 2.6) J/(kg·K) during lattice contraction (Fig. 1(f)), contributing cooperatively about 49% to the total entropy change 14.2 J/(kg·K) obtained by using Maxwell relation for $LaFe_{11.6}Si_{1.4}$ at a 0–1 T magnetic field. This result was also verified by their DFT calculation results. Moreover, Debye temperature calculated by Lamb-Mössbauer factor f_{LM} expressed a drop by about 4% from 363 K to 348 K upon heating (Fig. 1(g)). With Eq. (2) [62,63]

$$S_{\mathrm{Latt}} = 3Nk_{\mathrm{B}}\ln\left[1-\exp\left(-\frac{\theta}{T}\right)\right] + 12Nk_{\mathrm{B}}\left(\frac{T}{\theta}\right)^3\int_0^{\theta/T}\frac{x^3}{e^x-1}\mathrm{d}x, \tag{2}$$

where N is Avogadro constant, and θ is Debye temperature. A rise in the lattice entropy is indicated by the decrease in Debye temperature. The study conducted by Hao et al. on $La(Fe_{0.92}Co_{0.08})Si_{1.1}$ suggested that there was a drop of Debye temperature by about 3% during the transition from the FM phase to the PM phase (Fig. 1(h)) [64], thus evidencing that the sign of lattice and spin

entropy changes was the same in $La(Fe,Si)_{13}$-based compounds [64]. The sign problem still needs further investigation in more materials to obtain a convincingly general conclusion.

2.2 Amplitude

There are variant kinds of multicaloric materials, consisting of electric-structural, electric-magnetic, and magnetic-structural couplings. Herein, magnetic-structural coupling materials, i.e., materials with a magnetostructural/magnetoelastic transition will be concentrated on. For the entropy change during this transition, lattice (ΔS_L) and spin (ΔS_M) entropy changes play the most important part, considering the fact that the contribution of electronic entropy is generally neglectable at high temperatures. Theoretically, the maximum ΔS_M, $Rln(2J+1)$ where J is the total angular momentum quantum number, imposes restrictions on spin entropy changes and ΔS_L reflects the internal entropy change which can be partially implied by lattice volume changes. Therefore, enlarging ΔS_L is an effective path to enhancing caloric effects [66]. Nonetheless, applying distinct magnitude of magnetic fields, ΔS_L cannot be enhanced for general magnetocaloric materials with a magnetostructural transition, such as $Gd_5Si_2Ge_2$ whose ΔS_L decreases from 10.6 J/(kg·K) to 9.2 J/(kg·K) while the magnetic field (H) increases from 0–2 T to 0–10 T and $Gd_5Si_{2.09}Ge_{1.91}$ with a ΔS_L of 9.2 (± 0.2) J/(kg·K) nearly unchanged while an H changing from 0–2 T to 0–5 T [66–68].

Hao et al. reported that with the employed pressure influencing spin fluctuations and specific Fe-Fe bonds, the negative volume expansion was increased and the magnetoelastic transition was sharpened, hence increasing the entropy change to 1.8 times at a magnetic field change of 0–5 T with a pressure of 11.31 kbar applied as large as that under 0 kbar for $La(Fe_{0.92}Co_{0.08})_{11.9}Si_{1.1}$ [64]. However, the mechanism mentioned above strengthens the first-order nature and introduces more hysteresis losses. Therefore, Hao et al. found another mechanism in HoCuSi compounds. With the physical pressure impacting the distance between Ho atoms and lattice parameters, crystal field interactions and magnetic exchange interactions were influenced. The AFM ground state with a sine wave modulated spin structure was changed in HoCuSi. Although the exact spin structure driven by pressure was unknown, the magnetization process became easily saturated and the effective magnetic moment was slightly enhanced. As a result, the entropy change was enhanced by 150% at a low magnetic field change of 0–1 T without adding additional hysteresis losses [69].

For $La(Fe_{0.92}Co_{0.08})_{11.9}Si_{1.1}$ compounds, as the pressure increases, the transition temperature decreases (dT_C/dP = −7 K/kbar), and the transition becomes sharper: the full width at half maximum (FWHM) is lowered from 23.1 K to 6.7 K and the peak of dM/dT rises from 3.8 to 16.3 $A·m^2/(kg·K)$ with the pressure applied rising from 0 to 11.31 kbar [64] (Fig. 2(a)). The Arrott plots show that with physical pressure increasing from 0 to 11.31 kbar, the transition generally evolved from a second order to a first order, introducing hysteresis (Fig. 2b). Figure 2(e) reveals that the total entropy change was improved by 0.8 times higher from 14.1 to about 26.0 J/(kg·K) at a field change of 0–5 T with the applied pressure rising from 0 to 11.31 kbar. Employing variable temperature neutron powder diffraction (NPD) at different pressures, the volume and parameters of the lattice were determined (Figs. 2(c), 2(d), 2(f)). The negative volume expansion was enhanced from −1.08% to −1.57% when the pressure was applied up to 9 kbar while correspondingly, the amplitude of the shrinkage of the intra-icosahedron Fe−Fe bonds B1, B2, and B3 simultaneously increased with the symmetry of the icosahedron almost unchanged under pressure. This can be attributed to the magnetoelastic softening, though the lattice volume contracts. The PM phase is more sensitive to pressure than the FM phase, leading to a boost in the negative lattice expansion. To conclude, the applied pressure enlarges volume changes, increasing lattice entropy changes (ΔS_L). Therefore, it results in an obvious boost of magnetocaloric effects by multifield tuning. The total entropy change of the magnetocaloric effect is almost doubled at a pressure of 11.31 kbar with the H changing from 0 to 5 T (Fig. 2(e)). The first-principles calculations were performed, which offered theoretical support for the enlarged caloric effects related to the evolution of phase transition nature. Moreover, the enhanced lattice entropy change was calculated by Debye approximation and a reliable way to evaluate barocaloric effect at a high pressure that DSC cannot reach was demonstrated [64].

Former research indicated that the Neel temperature of HoCuSi is about 9 K, below which it shows an AFM ground state where Ho^{3+} ions form a sin wave modulation spin structure possessing a propagation vector k = (1/15, 0, 1/6) [70]. With powder X-ray diffraction (XRD) exploring the crystal structure, Fig. 3(a) gives the Rietveld refined XRD pattern which shows that the sample possesses a Ni_2In-type hexagonal structure with a space group $P6_3/mmc$ at room temperature. Figure 3(b) suggests that pressure favored the FM interaction. Therefore, the PM Curie temperature rose from 3.6 to 8.2 K and the effective moment M_{eff} rose from 10.07 μ_B/Ho^{3+} to about 10.59 μ_B/Ho^{3+} with pressure increasing from 0 to 9 kbar [69]. Figures 3(c)–3(e) implie that the sample at a higher pressure possesses a lower critical field triggering the transition from the AFM phase to the FM phase and there is no hysteresis no matter what pressure is applied. The reduced distance between Ho atoms by applying physical pressure may increase FM couplings

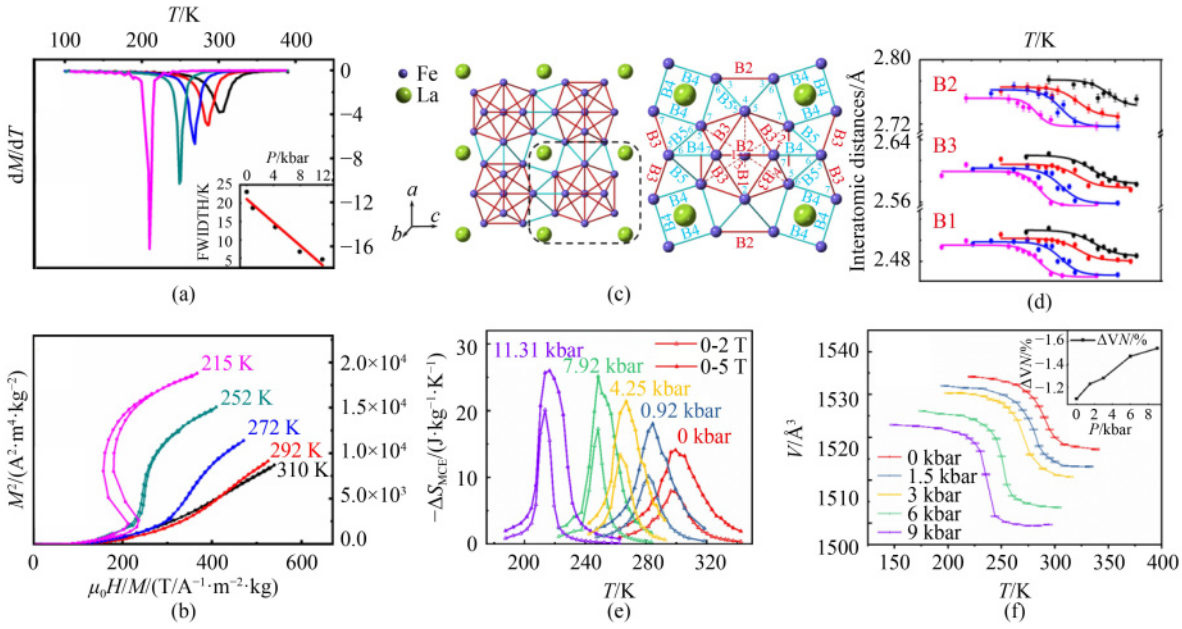

Fig. 2 Amplitude tuned by multifield for $La(Fe_{0.92}Co_{0.08})_{11.9}Si_{1.1}$ compounds.

(a) d*M*/d*T*-*T* curves in the magnetic field 1 T at different pressures where the inset denotes FWHMs at different pressures (reprinted with permission from Ref. [64], Copyright 2020, American Chemical Society); (b) corresponding Arrott plots (reprinted with permission from Ref. [64], Copyright 2020, American Chemical Society); (c) two-dimension diagram of the partial lattice structure of $La(Fe,Si)_{13}$ compounds (reprinted with permission from Ref. [64], Copyright 2020, American Chemical Society); (d) changes of intra-icosahedron Fe-Fe bonds B1, B2, and B3 with the variation of temperature at different pressures (reprinted with permission from Ref. [64], Copyright 2020, American Chemical Society); (e) applied variant pressure, the temperature dependence of the isothermal entropy change with the magnetic field changing from 0 to 2 T/5 T (reprinted with permission from Ref. [64], Copyright 2020, American Chemical Society); (f) lattice volume [64] (reprinted with permission from Ref. [64], Copyright 2020, American Chemical Society).

(magnetic exchange interactions) and alter crystal field interactions, thus impacting the non-collinear sin wave modulated spin structure and obtaining a higher M_{eff}. Consequently, the magnetization process is altered, and the entropy change can be enhanced by 150% from 4.8 to 12 J/(kg·K) at a low magnetic field of 1 T by introducing a hydrostatic pressure of 6.6 kbar (Fig. 3 (b)). This mechanism does not introduce hysteresis (Figs. 3(c)–3(e)).

2.3 Temperature transition span

Since the discovery of first-order transition materials with giant caloric effects, like $Gd_5Si_2Ge_2$ [34,35], FeRh [36,37], $La(Fe,Si)_{13}$ [38,41], and MnAs [42,52], they have drawn much attention [18,22,71–75]. Compared to the traditional caloric material Gd with a second order transition, they have unprecedented large entropy changes but the sharp transition in these materials generally leads to a narrow transition temperature span which limits their practical applications [2]. Variant methods have been tried to solve this problem on bulk materials, consisting of nanostructuring, introducing chemical pressure, and applying hydrostatic and uniaxial pressure, acquiring progress to some extent [3,41,76–79]. Recently, Qiao et al. applied multifield to broaden the temperature range of FeRh films, proposing a novel method for tailoring the transition temperature span [80].

Previous studies indicated that the transition from the AFM phase to the FM phase in FeRh alloys with the cubic structure upon heating is a first-order transition together with a volume expansion of about 1%. Therefore, this transition can be driven by either magnetic fields or stresses [36,37]. Grown on the (001) direction of relaxor ferroelectric single crystals $0.7Pb(Mg_{1/3}Nb_{2/3})O_3$-$0.3PbTiO_3$ (PMN-PT), spontaneously polarizing along the 8 orientations of rhombohedral body diagonals (Fig. 4(a)), the (011) orientational FeRh film could be impacted by strains induced by the mismatch which was buffered by the formation of AB_2O_4 spinel layers. Obeying the principle of minimum energy, the energy of distortions and strains would be reduced by the variation of FeRh lattices. The multidomain characteristics of the PMN-PT substrate led to the domain division of the FeRh film, as exhibited in Fig. 4(b). Domain A and domain B bore different strains, the phase transition temperature of which appeared at different positions. Since compression stabilizes the AFM phase and stretching stabilizes the FM phase, domain A with compressive strains and B with tensile strains caused a two-step phase transition either in the heating or the cooling process (Fig. 4(c)). When the electric field of + 8 kV/cm was applied along the [001] direction of the PMN-PT substrate, the 109° domain switching boosted

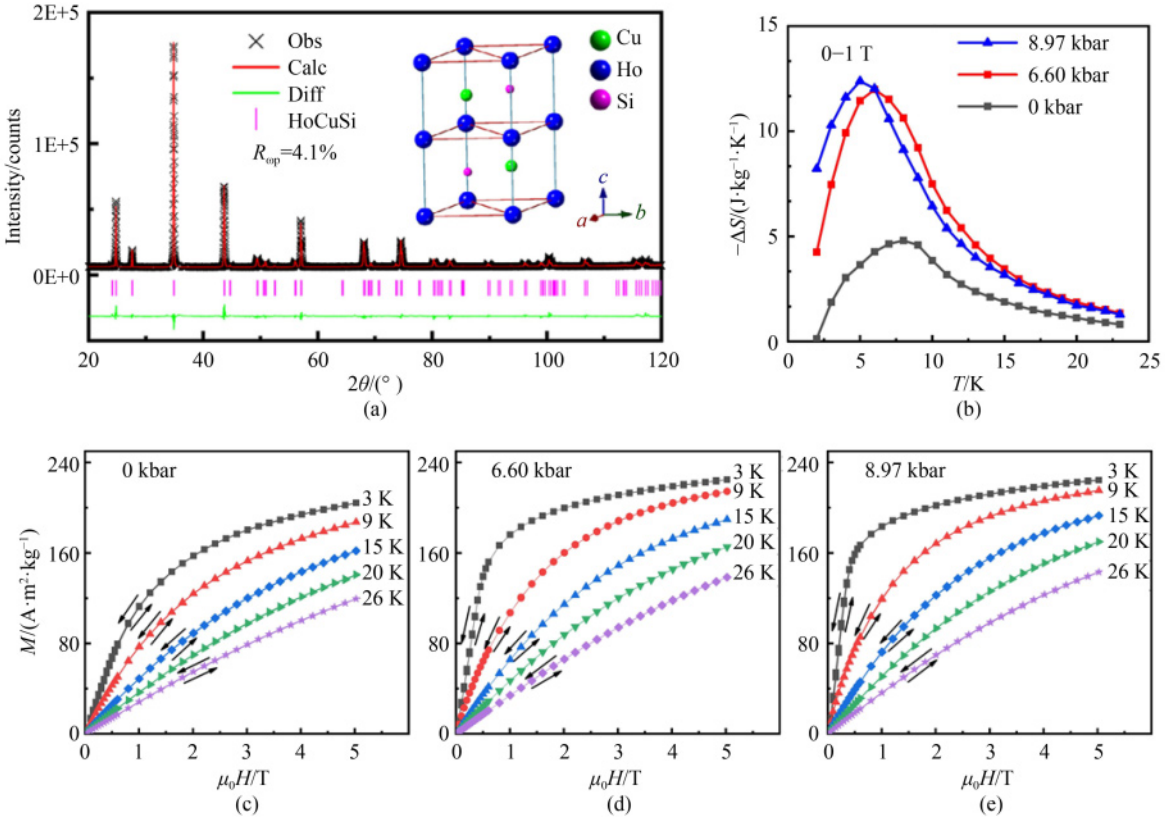

Fig. 3 Amplitude tuned by multifield for HoCuSi compounds.

(a) Room temperature Rietveld refined XRD diagram where the inset shows the lattice structure (reprinted with permission from Ref. [69], Copyright 2020, Elsevier); (b) isothermal entropy change as a function of temperature at the 0–1 T magnetic field at different pressures (reprinted with permission from Ref. [69], Copyright 2020, Elsevier); (c) *M-H* curves at a pressure of 0 kbar (reprinted with permission from Ref. [69], Copyright 2020, Elsevier); (d) *M-H* curves at a pressure of 6.60 kbar; (e) *M-H* curves at a pressure of 8.97 kbar [69] (reprinted with permission from Ref. [69], Copyright 2020, Elsevier).

the ratio of domain A, enlarging the peak of domain A while for −8 kV/cm, besides 109° transforming the same as that under the positive field, the 71°/180° domain switching introduced large compressive strains (Fig. 4(d)). Therefore, the peak of domain A was enlarged and the transition temperature of domain B was lifted, leading to an emergence of two peaks (inset of Fig. 4(c)). With electric fields tuning the transition temperature, the cooling temperature span would be dynamically broadened to 60 K (Fig. 4(e)). Employing suitable multifield tuning, this widened cooling temperature span can be used in cooling devices [80].

2.4 Hysteresis

Besides the narrow transition temperature span, another obstacle to the application of caloric materials with a first-order transition is hysteresis. Hysteresis losses refer to the meaningless energy losses induced by the internal properties of materials instead of energy consumed by an actuating system which can be reduced or even eliminated by subtle mechanism designs. Therefore, it is a straightforward way to raise the working efficiency of a prototype by decreasing hysteresis losses. To put materials with a first-order transition into use, researchers have attempted to minimize hysteresis losses by doping, introducing porosity or hydrostatic pressure [72,81,82], of which the most successful one is the Heusler alloys NiMnCoIn tuned by multifield (magnetic fields and hydrostatic pressure) [72]. In addition, Qiao et al. showed that the hysteresis loss of FeRh films could be minimized, even reversed by the cooperation of electric and magnetic fields [73] for the FeRh films grown on PMN-PT substrates, which filled the blank of the film tuning aiming at reducing hysteresis.

The FeRh film was grown on the PMN-PT single crystal substrate with the (011) orientation. A magnetic field drives a transition from the AFM phase to the FM phase with a lattice volume expansion of about 1% [36]. Applying a negative electric field on PMN-PT substrates would introduce compressive strains which stabilize the AFM phase, decreasing magnetization. The memory effect in PMN-PT substrates prevented the strain from disappearing unless a positive electric field was employed to drive it back to the original state and the memory effect again kept it unchanged with the positive

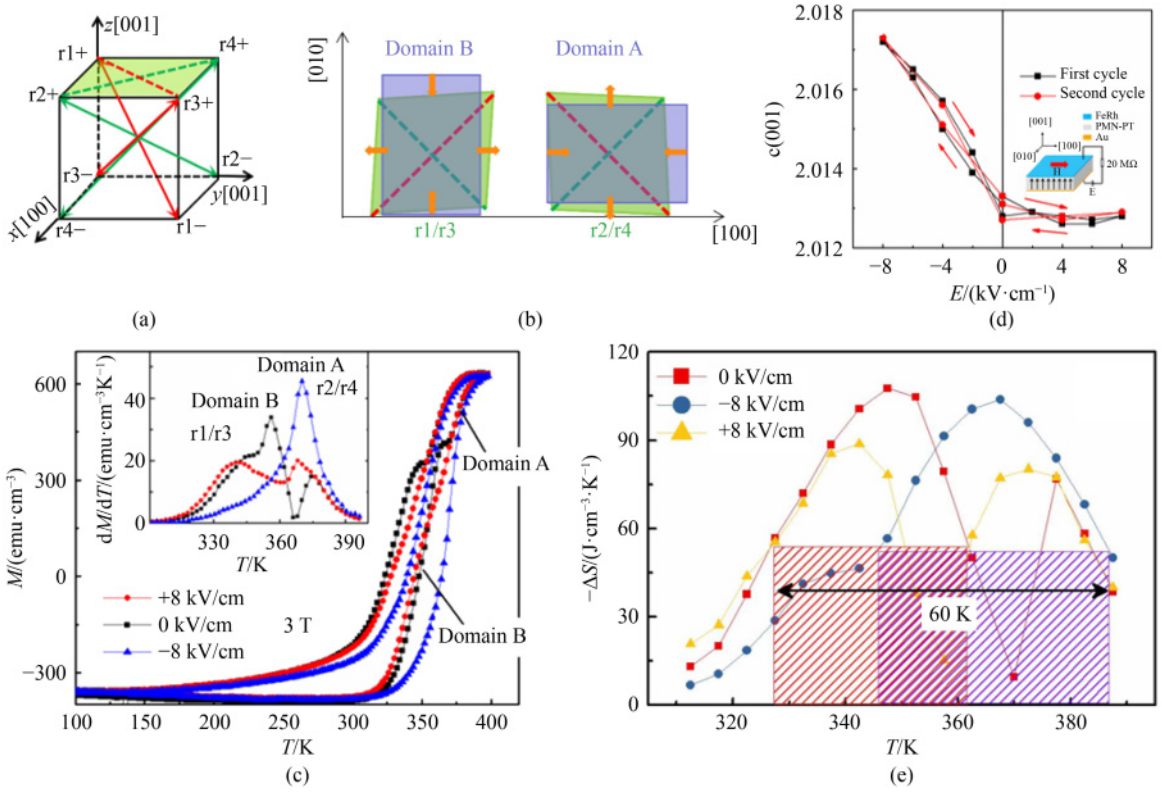

Fig. 4 Temperature transition range tuned by multifield for FeRh(011)/PMN-PT (001) heterojunction.

(a) Schematic of the 8 spontaneous polarization vectors for (001)-oriented PMN-PT single crystals (reprinted with permission from Ref. [80], Copyright 2020, Elsevier); (b) projections of ferroelectric domains and corresponding FM domains of FeRh in the (001) plane of the PMN-PT, i.e., the (011) plane of FeRh (reprinted with permission from Ref. [80], Copyright 2020, Elsevier); (c) change of magnetization with variation of temperature measured at a 3 T magnetic field with *in situ* electric fields of 0, +8 and −8 kV/cm (reprinted with permission from Ref. [80], Copyright 2020, Elsevier); (d) electric field dependence of lattice parameter along the [001] direction of PMN-PT (reprinted with permission from Ref. [80], Copyright 2020, Elsevier); (e) temperature dependence of isothermal entropy change in different electric fields [80] (reprinted with permission from Ref. [80], Copyright 2020, Elsevier).

field removed. As a result, the magnetization curve a–b was replaced by the curve c–d (Fig. 5(b)), with a pulse electric field applied only at both ends of magnetic fields (0, H) rather than the magnetization/demagnetization process, leading to a decrease in hysteresis losses (Figs. 5(a)–5(b)). Because the domain switching of PMN-PT substrate cannot provide enough memorable compressive strains, the irreversible rhombohedral-to-orthorhombic (R-O) phase transition was taken advantage of to produce compressive strains as much as −0.45% along the in-plane [100] direction [73]. The *M-E* loop and XRD patterns at room temperature proved that there indeed existed the strain memory effect during the phase transition (Figs. 5(c) and 5(e)). Compared to Fig. 5(f) which expresses a magnetization curve without the participation of the electric field, Fig. 5(g) gives the case with the electric field applied. With the pulse electric field ±6 kV/cm applied at 0 and 5 T magnetic fields at 320 K, the measured hysteresis loss was reduced by 58% with an in-plane strain of −0.20%. Furthermore, with a larger pulse electric field, the hysteresis loss is expected to be eliminated when the introduced compressive strain reaches up to −0.35%, even reversed (strain over −0.35%). All in all, different from the mechanism used before, the decrease of hysteresis in FeRh films is due to the conversion of electric energy, i.e., whether the working efficiency can be improved depends on conversion efficiency, and the internal properties of materials are not changed at all. But hopefully, this work opens a new path for promoting SCP by applying multifield.

2.5 Coupled-caloric effect

Based on the theory of thermodynamics, multicaloric and coupled-caloric effects can be expressed by the isothermal entropy change with Eq. (3) [49]

$$\begin{aligned}\Delta S\left[T,(0,0)\rightarrow(x_1,x_2)\right]=&\int_0^{x_1}\left(\frac{\partial y_1}{\partial T}\right)_{x_1,x_2=0}\mathrm{d}x_1\\&+\int_0^{x_2}\left(\frac{\partial y_2}{\partial T}\right)_{x_1=0,x_2}\mathrm{d}x_2\\&+\int_0^{x_1}\int_0^{x_2}\frac{\partial x_{12}}{\partial T}\mathrm{d}x_2\mathrm{d}x_1,\end{aligned}\quad(3)$$

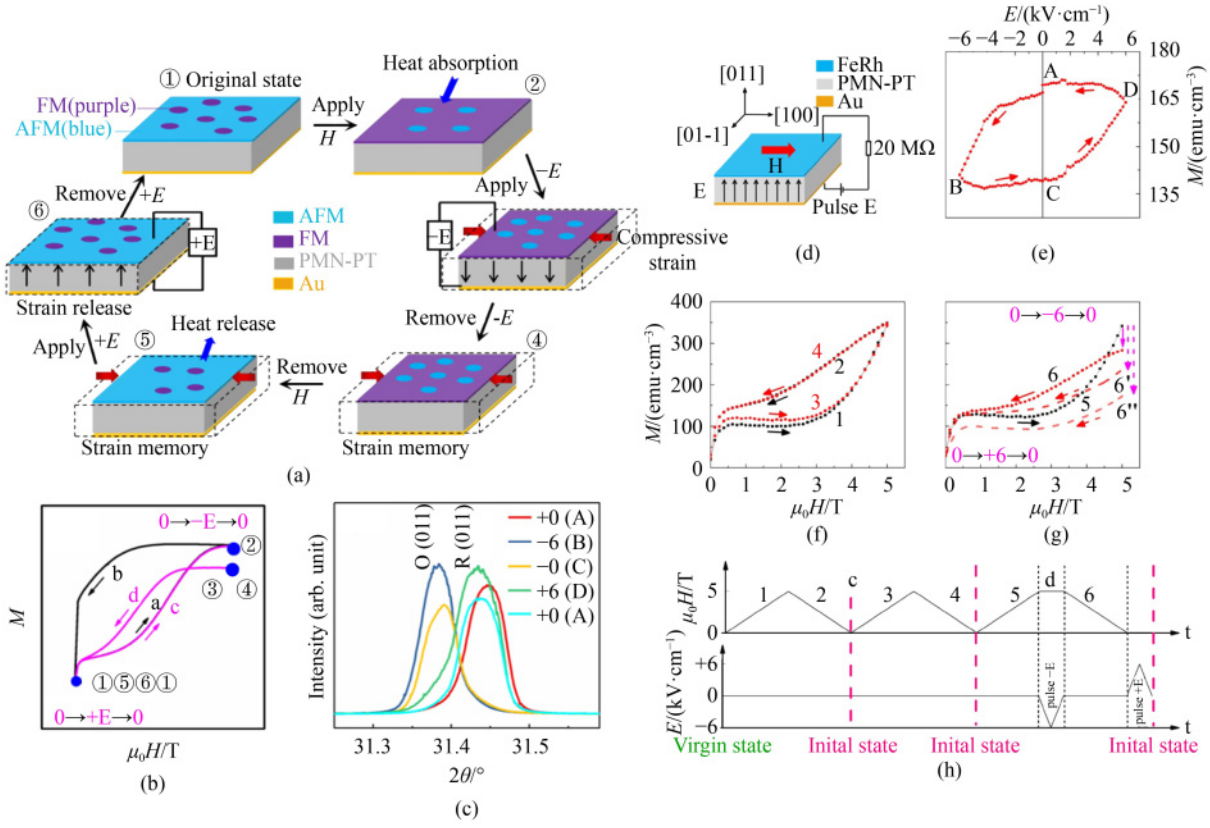

Fig. 5 Hysteresis tuned by multifield for FeRh/PMN-PT (011) heterojunction.

(a) Schematic of the working principle of refrigeration (reprinted with permission from Ref. [73], Copyright 2019, Elsevier); (b) corresponding M-H curves in which the pulse electric field is applied at both ends of the magnetic field 0, *H* (reprinted with permission from Ref. [73], Copyright 2019, Elsevier); (c) room temperature XRD pattern of the PMN-PT with electric fields *in situ* applied in the sequence of +0, −6, −0, +6, and +0 kV/cm (reprinted with permission from Ref. [73], Copyright 2019, Elsevier); (d) schematic of the heterostructure with magnetic and pulse electric fields (reprinted with permission from Ref. [73], Copyright 2019, Elsevier); (e) magnetization at 310 K in the magnetic field 5 T as a function of electric field (reprinted with permission from Ref. [73], Copyright 2019, Elsevier); (f) *M-H* curves (reprinted with permission from Ref. [73], Copyright 2019, Elsevier); (g) *M-H* curves with the application of a pulse electric field at 0, 5 T where curves 5 and 6 denote the application of the pulse electric field 6 kV/cm and others denote predicted process with larger pulse fields (reprinted with permission from Ref. [73], Copyright 2019, Elsevier); (h) schematic of the time sequence of the application of pulse electric and magnetic fields [73] (reprinted with permission from Ref. [73], Copyright 2019, Elsevier).

where the summation denotes the multicaloric effect, the first and second items on the right of the equation denote single caloric effects, the last one denotes the coupled-caloric effect, y_i denotes ferroic order parameters, x_i denotes the conjugated fields, and T denotes temperature (more details can be seen in Ref. [49]). By now, a large part of studies about the coupled-caloric effect have been concentrated on the cooperation between hydrostatic pressure and magnetic/electric fields while a few focused on the union of electric and magnetic fields.

$Fe_{49}Rh_{51}$ alloys undergo a transition from the AFM phase to the FM phase together with a volume expansion of about 1%. Therefore, it is possible to study the coupled-caloric effect on this material [83,84]. Stern-Taulats et al. surveyed the *M-P* curves of $Fe_{49}Rh_{51}$ and further calculated isothermal entropy changes based on magnetic measurements under pressure [83] (Fig. 6(a)). To optimize the performance of caloric effects, the applied magnetic field and pressure were in opposite directions, amazingly attaining a wide transition temperature span of about 50 K by the coupled-caloric effect. Besides, the fields applied in the same direction, which caused the competition between the inverse magnetocaloric effect and the normal barocaloric effect, were also investigated (Fig. 6(b)). With the magnitude of the magnetic field applied increasing from 0 to 5 T, the inverse magnetocaloric effect generally dominated the process and the transition temperature moved to lower temperatures because magnetic fields favored the FM phase while pressure did the other. Thus, by the function of the coupled-caloric effect, the transition temperature and the sign of entropy change can be controlled, providing convenience for optimizing the performance of caloric effects. However, the principle causing coupled-caloric effects is not discussed in this work, calling for deeper research.

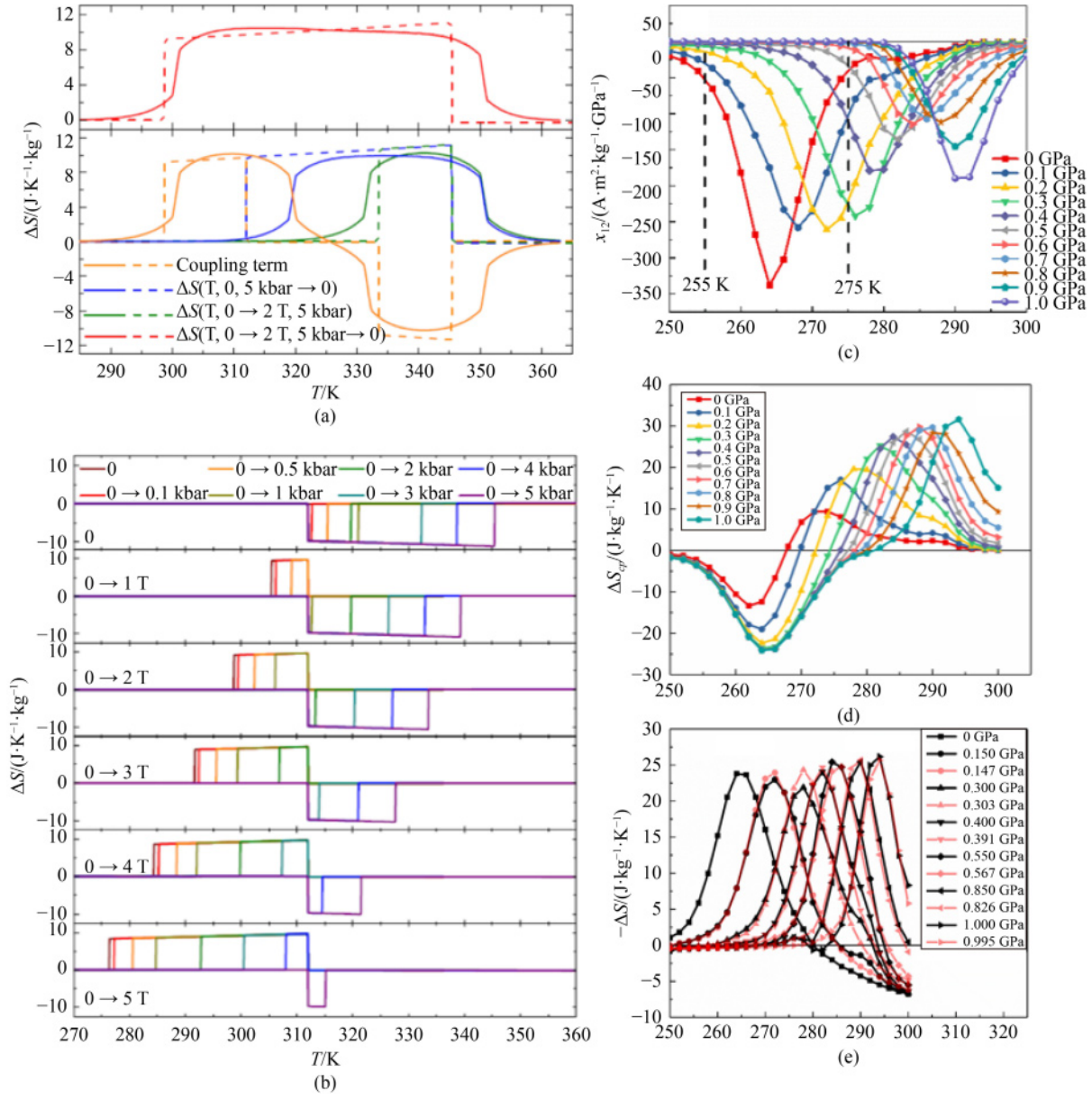

Fig. 6 Coupled-caloric effects.

(a) Various isothermal entropy changes as a function of temperature of the process applying a field 2 T or removing pressure 5 kbar for FeRh alloys [83] (reprinted with permission from Ref. [83], Copyright 2017, American Physical Society); (b) multicaloric isothermal entropy change as a function of temperature of the process applying the magnetic field and pressure of different magnitude [83] (reprinted with permission from Ref. [83], Copyright 2017, American Physical Society); (c) temperature dependence of the magnetic volume coupling coefficient χ_{12}at a magnetic field 5 T at different pressures for $Ni_{50}Mn_{35}In_{15}$ [86]; (d) temperature dependence of the coupling isothermal entropy change with the field change from 5 to 0 T at different pressures for $Ni_{50}Mn_{35}In_{15}$ [86]; (e) comparison of the total entropy change obtained by the adjustment of the coupling isothermal entropy change on the isothermal magnetocaloric entropy change in ambient pressure (black) and the isothermal magnetocaloric entropy change at selected pressure computed by Maxwell relation (red) [86].

Upon cooling, Heusler alloys $Ni_2Mn_{1+x}M_{1-x}$ (M = Ga, Sn and In, $0 < x < 1$) undergo a transition from the PM austenitic phase to the FM austenitic phase then to the AFM martensitic phase [84]. Since the AFM phase possesses a smaller lattice volume than the FM phase, hydrostatic pressure favors the AFM phase by boosting the AFM exchange interaction between Mn atoms by reducing the distance between them [85]. Thus, $Ni_2Mn_{1+x}M_{1-x}$ is an ideal material to study coupled-caloric effects [86]. Figure 6(c) presents the magnetic volume coupling coefficient χ_{12} calculated by M-P curves measured at variant temperatures. By integrating χ_{12}, the coupled-caloric effect was attained which exhibited two separated peaks (Fig. 6(d)). By comparing the isothermal entropy change calculated by the two methods, the equivalence between the magnetocaloric effect at a

certain pressure and the addition of the magnetocaloric effect at ambient pressure and the relevant coupled caloric effect were further proved (Fig. 6(e)). Corporately, the negative and positive peaks pushed the total entropy change peak to a higher temperature of about 294 K (about 30 K higher) and a larger value of 25.7 J/(kg·K) (which is enhanced by 8%) with the applied pressure increasing from zero to 9.95 kbar at a magnetic field changing from 5 to 0 T. Hence, the magnitude of the entropy change and the transition temperature can be adjusted by the coupled-caloric effect. However, deep mechanisms have not been revealed yet [49].

2.6 Other progress

Caloric materials with a larger SCP (SCP = $C\Delta T_{ad}f$, where C is specific heat capacity, ΔT_{ad} is the adiabatic temperature change of material, and f is the frequency of alternating magnetic fields) driven by low fields are what researchers pursue. In addition, the reversibility of caloric effects during cooling circulations is also important. Qiao et al. reported that by introducing second phases, FeRh alloys had an improved adiabatic temperature change ΔT_{ad} of about 0.48 K, 70% larger than monophase FeRh under a low magnetic field of 0.62 T with an alternating frequency of 1 Hz, and the cycling stability was elevated [87]. XRD patterns revealed that except the α-FeRh phase, there existed the second phases containing 4.6% α-Fe and 2.4% γ-FeRh phases (Fig. 7(a)). Lorentz TEM images indicated that in the low-temperature AFM phase, there were small FM domains which were formed by the dominant phase, the α-FeRh phase (Fig. 7(b)). The adiabatic temperature change ΔT_{ad} of about 4.8 K decreased by 14% to 4.1 K after long cycles in the 1.8 T,

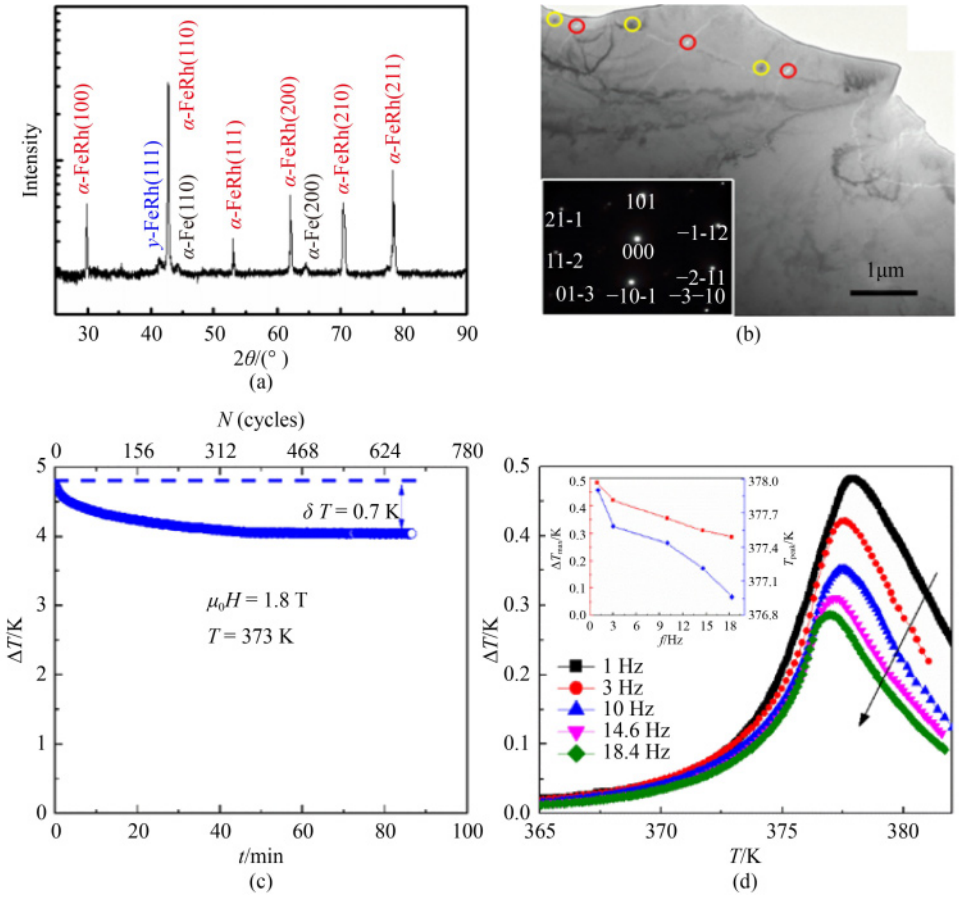

Fig. 7 Performance tuned by introducing second phases for FeRh alloys.

(a) Room temperature XRD pattern of the FeRh sample (reprinted with permission from Ref. [87], Copyright 2022, American Chemical Society); (b) room temperature under-focused Lorentz transmission electron microscopy (TEM) where the inset shows the selected area electron diffraction along the [1, −3, −1] direction of the α-FeRh phase (reprinted with permission from Ref. [87], Copyright 2022, American Chemical Society); (c) applying a 1.8 T, 0.13 Hz alternating magnetic field at 373 K, the adiabatic temperature change for FeRh alloys as a function of time and the number of magnetic field cycles (reprinted with permission from Ref. [87], Copyright 2022, American Chemical Society); (d) adiabatic temperature change as a function of temperature in a 0.62 T alternating magnetic field with variant frequencies where the inset shows the value and position of the peak as a function of frequency [87] (reprinted with permission from Ref. [87], Copyright 2022, American Chemical Society).

0.13 Hz alternating magnetic field, exhibiting a better cycling stability than studies before (usually 40%–50%) [88,89] (Fig. 7(c)). The local stress and stray magnetic field caused by the second phases impacting the energy distribution should recede the function of domain walls, which would account for the improved cycling stability [90–92]. Moreover, the lowered driving field should be attributed to the second phases promoting nucleation formation. Figure 7(d) revealed that with a low magnetic field 0.62 T, the temperature change was 0.48 K, 70% bigger than that in FeRh with a single phase reported before [93].

In addition, Gao et al. [33] and Seo et al. [94] independently found a giant reversible barocaloric effect triggered by low pressure in $(CH_3{-}(CH_2)_{n-1}{-}NH_3)_2MnCl_4$ organic-inorganic hybridization materials [95] with a layered perovskite structure. The single crystal sample $(CH_3{-}(CH_2)_{n-1}{-}NH_3)_2MnCl_4$ (n=10) exhibited thermal hysteresis as small as 2.6 K (inset of Fig. 8(a)). Different layers were linked by van der Waals force, while in the same layer "carbon chain"-"inorganic group"-"carbon chain" stacked together by hydrogen bonds (N−H···Cl) (Fig. 8(a)). SC-XRD and infrared spectra at selected temperatures revealed that during the transition, carbon chains underwent a melting process from a settled structure to an unconstrained state, which should claim for the large entropy change (Figs. 8(b)–8(e)). Gao et al. also believed that the absence of grain boundaries in the single crystal together with the special hybrid structure might explain the large reversible barocaloric effect of about 230 J/(kg·K) induced by a small field 0.08 GPa (Figs. 8(f), 8(g)). Figures 8(h) and 8(i) display that in comparison to other work, the superiority of this material focuses on low driving fields. In addition, Seo et al. discovered a similar phenomenon in $(NA)_2CuBr_4$ (NA = nonylammonium) [94].

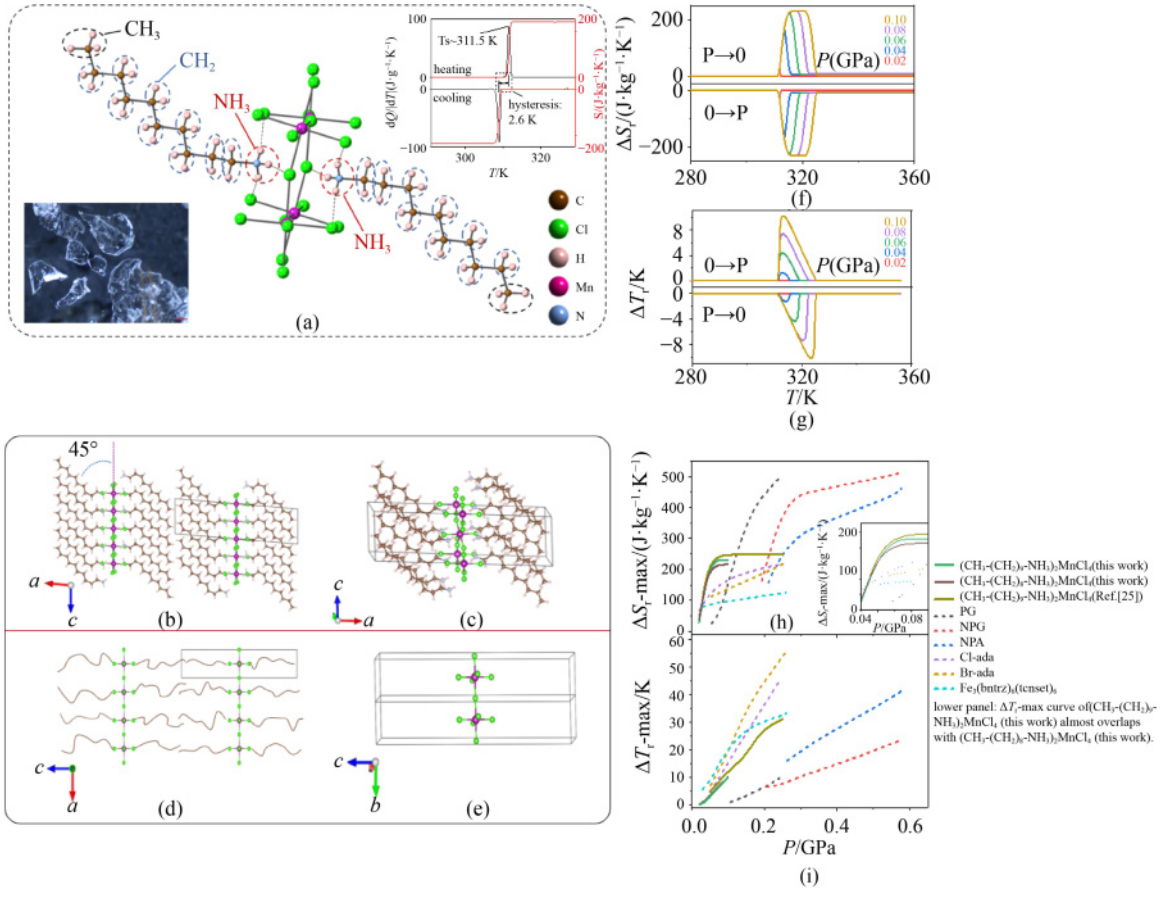

Fig. 8 Materials with a giant reversible barocaloric effect triggered by low pressure.

(a) Schematic of the molecular structure of $(CH_3{-}(CH_2)_{n-1}{-}NH_3)_2MnCl_4$ (n = 10) at 298 K where the carbon chains are connected to the inorganic group through N−H···Cl hydrogen bonds, (the left inset shows the morphology of the crystal, and the right inset shows dQ/dT-T curves recorded by DSC upon cooling and heating); (b) layer structure; (c) monoclinic lattice of the organic-inorganic-organic material observed along b axis at 298 K; (d) structure possessing melted carbon chains with various configurations observed along b axis; (e) tetragonal lattice observed along a axis at 320 K; (f) reversible isothermal entropy change calculated by the overlap of applying and removing pressure for the single crystal; (g) adiabatic temperature change attained by eliminating the impact of thermal hysteresis [30,96] as a function of temperature with different pressure changes for the single crystal; (h) maximal reversible isothermal entropy change; (i) adiabatic temperature change as a function of pressure of this study and previous studies [33].

3 Conclusions

To face the challenge of replacing traditional refrigerants with caloric materials, multifield tuning and multicaloric materials come into sight. By applying variant fields, many improvements can be achieved, such as reducing hysteresis losses, improving the magnitude of entropy changes, adjusting transition temperatures, and broadening transition temperature spans. Therefore, this is a potential method for further promoting the application of caloric materials. Other methods like hybridizing organic-inorganic materials and introducing second phases are also promising for improving caloric performance. However, there are still many things waiting for researchers to explore. Till now, the research on coupled-caloric effects has mainly been focused on materials with magnet-structural couplings, and a few on electric-structural and electric-magnetic couplings by theoretical means. In addition, cooling prototypes utilizing multifield are still at the early stage. Furthermore, the underlying mechanism of the coupling between different ferro-orders still requires further investigation for different materials. The new phonon evolution mechanism found during the investigation on the sign of spin and lattice entropy changes in $La(Fe,Si)_{13}$ compound means there are more unrevealed, calling for further studies.

Competing interests The authors declare that they have no competing interests.

Acknowledgements This work was supported by the National Key R&D Program of China (Grant Nos. 2020YFA0711502, 2021YFB3501202, 2019YFA0704900, 2018YFA0305704, and 2022YFB3505201), the National Natural Sciences Foundation of China (Grant Nos. 52088101, 92263202, 51971240, and 52101228), and the Strategic Priority Research Program B (Grant No. XDB33030200) and the Key Research Program (Grant Nos. ZDRW-CN-2021-3, 112111KYSB20180013) of the Chinese Academy of Sciences (CAS).

References

1. Gschneidner K A Jr, Pecharsky V K, Tsokol A O. Recent developments in magnetocaloric materials. Reports on Progress in Physics, 2005, 68(6): 1479–1539
2. Franco V, Blazquez J S, Ipus J J, et al. Magnetocaloric effect: From materials research to refrigeration devices. Progress in Materials Science, 2018, 93: 112–232
3. Shen B G, Sun J R, Hu F X, et al. Recent progress in exploring magnetocaloric materials. Advanced Materials, 2009, 21(45): 4545–4564
4. Zheng X Q, Shen B G. The magnetic properties and magnetocaloric effects in binary R-T (R = Pr, Gd, Tb, Dy, Ho, Er, Tm; T = Ga, Ni, Co, Cu) intermetallic compounds. Chinese Physics B, 2017, 26(2): 027501
5. Li L, Yan M. Recent progress in the development of $RE_2TMTM'O_6$ double perovskite oxides for cryogenic magnetic refrigeration. Journal of Materials Science and Technology, 2023, 136: 1–12
6. Zhang Y, Tian Y, Zhang Z, et al. Magnetic properties and giant cryogenic magnetocaloric effect in B-site ordered antiferromagnetic Gd_2MgTiO_6 double perovskite oxide. Acta Materialia, 2022, 226: 117669
7. Zhang Y, Zhu J, Li S, et al. Magnetic properties and promising magnetocaloric performances in the antiferromagnetic $GdFe_2Si_2$ compound. Science China Materials, 2022, 65(5): 1345–1352
8. Zhang Y K, Wu J H, He J, et al. Solutions to obstacles in the commercialization of room-temperature magnetic refrigeration. Renewable & Sustainable Energy Reviews, 2021, 143: 110933
9. Li L W, Yan M. Recent progresses in exploring the rare earth based intermetallic compounds for cryogenic magnetic refrigeration. Journal of Alloys and Compounds, 2020, 823: 153810
10. Gao F, Sheng J, Ren W, et al. Incommensurate spin density wave and magnetocaloric effect in the metallic triangular lattice $HoAl_2Ge_2$. Physical Review. B, 2022, 106(13): 134426
11. Neese B, Chu B, Lu S G, et al. Large electrocaloric effect in ferroelectric polymers near room temperature. Science, 2008, 321(5890): 821–823
12. Qian X S, Han D L, Zheng L R, et al. High-entropy polymer produces a giant electrocaloric effect at low fields. Nature, 2021, 600(7890): 664–669
13. Ma R, Zhang Z, Tong K, et al. Highly efficient electrocaloric cooling with electrostatic actuation. Science, 2017, 357(6356): 1130–1134
14. Greco A, Masselli C. Electrocaloric cooling: A review of the thermodynamic cycles, materials, models, and devices. Magnetochemistry (Basel, Switzerland), 2020, 6(4): 67
15. Chen Y Q, Qian J F, Yu J Y, et al. An all-scale hierarchical architecture induces colossal room-temperature electrocaloric effect at ultralow electric field in polymer nanocomposites. Advanced Materials, 2020, 32(30): 1907927
16. Niu X, Jian X D, Gong W P, et al. Field-driven merging of polarizations and enhanced electrocaloric effect in $BaTiO_3$-based lead-free ceramics. Journal of Advanced Ceramics, 2022, 11(11): 1777–1788
17. Zou K L, Shao C C, Bai P J, et al. Giant room-temperature electrocaloric effect of polymer-ceramic composites with orientated $BaSrTiO_3$ nanofibers. Nano Letters, 2022, 22(16): 6560–6566
18. Tušek J, Engelbrecht K, Eriksen D, et al. A regenerative elastocaloric heat pump. Nature Energy, 2016, 1(10): 16134
19. Zhao Z, Guo W, Zhang Z. Room-temperature colossal elastocaloric effects in three-dimensional graphene architectures: an atomistic study. Advanced Functional Materials, 2022, 32(42): 2203866
20. Dang P, Ye F, Zhou Y, et al. Low-fatigue and large room-temperature elastocaloric effect in a bulk $Ti_{49.2}Ni_{40.8}Cu_{10}$ alloy. Acta Materialia, 2022, 229: 117802
21. Li D, Li Z, Zhang X, et al. Giant elastocaloric effect in Ni-Mn-Ga-based alloys boosted by a large lattice volume change upon the Martensitic transformation. ACS Applied Materials & Interfaces, 2022, 14(1): 1505–1518

22. Mañosa L, Planes A. Materials with giant mechanocaloric effects: Cooling by strength. Advanced Materials, 2017, 29(11): 1603607
23. Moya X, Mathur N D. Caloric materials for cooling and heating. Science, 2020, 370(6518): 797–803
24. Li B, Kawakita Y, Ohira-Kawamura S, et al. Colossal barocaloric effects in plastic crystals. Nature, 2019, 567(7749): 506–510
25. Li F B, Li M, Xu X, et al. Understanding colossal barocaloric effects in plastic crystals. Nature Communications, 2020, 11(1): 4190
26. Lin J, Tong P, Zhang X, et al. Giant room-temperature barocaloric effect at the electronic phase transition in $Ni_{1-x}Fe_xS$. Materials Horizons, 2020, 7(10): 2690–2695
27. Zhang K, Song R, Qi J, et al. Colossal barocaloric effect in carboranes as a performance tradeoff. Advanced Functional Materials, 2022, 32(20): 2112622
28. Ren Q, Qi J, Yu D, et al. Ultrasensitive barocaloric material for room-temperature solid-state refrigeration. Nature Communications, 2022, 13(1): 2293
29. Romanini M, Wang Y, Gurpinar K, et al. Giant and reversible barocaloric effect in trinuclear spin-crossover complex $Fe_3(bntrz)_6(tcnset)_6$. Advanced Materials, 2021, 33(10): 2008076
30. Aznar A, Negrier P, Planes A, et al. Reversible colossal barocaloric effects near room temperature in 1-X-adamantane (X = Cl, Br) plastic crystals. Applied Materials Today, 2021, 23: 101023
31. Imamura W, Usuda E O, Paixao L S, et al. Supergiant barocaloric effects in acetoxy silicone rubber over a wide temperature range: Great potential for solid-state cooling. Chinese Journal of Polymer Science, 2020, 38(9): 999–1005
32. Aznar A, Lloveras P, Barrio M, et al. Reversible and irreversible colossal barocaloric effects in plastic crystals. Journal of Materials Chemistry. A, Materials for Energy and Sustainability, 2020, 8(2): 639–647
33. Gao Y, Liu H, Hu F, et al. Reversible colossal barocaloric effect dominated by disordering of organic chains in $(CH_3\text{-}(CH_2)_{n-1}\text{-}NH_3)_2MnCl_4$ single crystals. NPG Asia Materials, 2022, 14(1): 34
34. Pecharsky V K, Gschneidner K A Jr. Giant magnetocaloric effect in $Gd_5(Si_2Ge_2)$. Physical Review Letters, 1997, 78(23): 4494–4497
35. Pecharsky V K, Gschneidner K A Jr. Effect of alloying on the giant magnetocaloric effect of $Gd_5(Si_2Ge_2)$. Journal of Magnetism and Magnetic Materials, 1997, 167(3): L179–L184
36. Nikitin S A, Myalikgulyev G, Tishin A M, et al. The magnetocaloric effect in $FE_{49}RH_{51}$ compound. Physics Letters. [Part A], 1990, 148(6–7): 363–366
37. Annaorazov M P, Nikitin S A, Tyurin A L, et al. Anomalously high entropy change in FeRh alloy. Journal of Applied Physics, 1996, 79(3): 1689–1695
38. Hu F X, Shen B G, Sun J R, et al. Influence of negative lattice expansion and metamagnetic transition on magnetic entropy change in the compound $LaFe_{11.4}Si_{1.6}$. Applied Physics Letters, 2001, 78(23): 3675–3677
39. de Oliveira N A. Giant magnetocaloric and barocaloric effects in $R_5Si_2Ge_2$ (R = Tb, Gd). Journal of Applied Physics, 2013, 113(3): 033910
40. Hu F X, Shen B G, Sun J R, et al. Great magnetic entropy change in La(Fe, $M)_{13}$ (M = Si, Al) with Co doping. Chinese Physics (Beijing), 2000, 9(7): 550–553
41. Fujita A, Fujieda S, Hasegawa Y, et al. Itinerant-electron metamagnetic transition and large magnetocaloric effects in $La(Fe_xSi_{1-x})_{13}$ compounds and their hydrides. Physical Review B: Condensed Matter, 2003, 67(10): 104416
42. Wada H, Tanabe Y. Giant magnetocaloric effect of $MnAs_{1-x}Sb_x$. Applied Physics Letters, 2001, 79(20): 3302–3304
43. UI Hassan N, Shah I A, Khan T, et al. Magnetostructural transformation and magnetocaloric effect in $Mn_{48-x}V_xNi_{42}Sn_{10}$ ferromagnetic shape memory alloys. Chinese Physics B, 2018, 27(3): 037504
44. Yang H, Liu J, Li C, et al. Ferromagnetism and magnetostructural coupling in V-doped MnNiGe alloys. Chinese Physics B, 2018, 27(10): 107502
45. Bao L F, Huang W D, Ren Y J. Tuning martensitic phase transition by non-magnetic atom vacancy in MnCoGe alloys and related giant magnetocaloric effect. Chinese Physics Letters, 2016, 33(7): 077502
46. Zhang H, Xing C F, Long K W, et al. Linear dependence of magnetocaloric effect on magnetic field in $Mn_{0.6}Fe_{0.4}NiSi_{0.5}Ge_{0.5}$ and $Ni_{50}Mn_{34}Co_2Sn_{14}$ with first-order magnetostructural transformation. Acta Physics Sinica, 2018, 67(20): 207501 (in Chinese)
47. Zhang B, Zheng X Q, Zhao T Y, et al. Machine learning technique for prediction of magnetocaloric effect in $La(Fe,Si/Al)_{13}$-based materials. Chinese Physics B, 2018, 27(6): 067503
48. Castillo-Villa P O, Soto-Parra D E, Matutes-Aquino J A, et al. Caloric effects induced by magnetic and mechanical fields in a $Ni_{50}Mn_{25-x}Ga_{25}Co_x$ magnetic shape memory alloy. Physical Review B: Condensed Matter and Materials Physics, 2011, 83(17): 174109
49. Hao J Z, Hu F X, Yu Z B, et al. Multicaloric and coupled-caloric effects. Chinese Physics B, 2020, 29(4): 047504
50. Pecharsky V K, Gschneidner K A Jr. Phase relationships and crystallography in the pseudobinary system Gd_5Si_4-Gd_5Ge_4. Journal of Alloys and Compounds, 1997, 260(1–2): 98–106
51. Hu F X, Gao J, Qian X L, et al. Magnetocaloric effect in itinerant electron metamagnetic systems $La(Fe_{1-x}Co_x)_{11.9}Si_{1.1}$. Journal of Applied Physics, 2005, 97(10): 10M303
52. Wada H, Matsuo S, Mitsuda A. Pressure dependence of magnetic entropy change and magnetic transition in $MnAs_{1-x}Sb_x$. Physical Review B: Condensed Matter and Materials Physics, 2009, 79(9): 092407
53. Liu E, Wang W, Feng L, et al. Stable magnetostructural coupling with tunable magnetoresponsive effects in hexagonal ferromagnets. Nature Communications, 2012, 3(1): 873
54. Zhao Y Y, Hu F X, Bao L F, et al. Giant negative thermal expansion in bonded MnCoGe-based compounds with Ni_2In-type hexagonal structure. Journal of the American Chemical Society, 2015, 137(5): 1746–1749
55. Johnson V. Diffusionless orthorhombic to hexagonal transitions in ternary silicides and germanides. Inorganic Chemistry, 1975, 14(5): 1117–1120
56. Anzai S, Ozawa K. Coupled nature of magnetic and structural

transition in MnNiGe under pressure. Physical Review B: Condensed Matter, 1978, 18(5): 2173–2178
57. Łażewski J, Piekarz P, Tobola J, et al. Phonon mechanism of the magnetostructural phase transition in MnAs. Physical Review Letters, 2010, 104(14): 147205
58. Jia L, Liu G J, Sun J R, et al. Entropy changes associated with the first-order magnetic transition in $LaFe_{13-x}Si_x$. Journal of Applied Physics, 2006, 100(12): 123904
59. Gruner M E, Keune W, Roldan Cuenya B, et al. Element-resolved thermodynamics of magnetocaloric $LaFe_{13-x}Si_x$. Physical Review Letters, 2015, 114(5): 057202
60. Landers J, Salamon S, Keune W, et al. Determining the vibrational entropy change in the giant magnetocaloric material $LaFe_{11.6}Si_{1.4}$ by nuclear resonant inelastic X-ray scattering. Physical Review. B, 2018, 98(2): 024417
61. Bao L F, Hu F X, Wu R R, et al. Evolution of magnetostructural transition and magnetocaloric effect with Al doping in $MnCoGe_{1-x}Al_x$ compounds. Journal of Physics. D, Applied Physics, 2014, 47(5): 055003
62. Li B, Ren W J, Zhang Q, et al. Magnetostructural coupling and magnetocaloric effect in Ni-Mn-In. Applied Physics Letters, 2009, 95(17): 172506
63. von Ranke P J, de Oliveira N A, Mello C, et al. Analytical model to understand the colossal magnetocaloric effect. Physical Review B: Condensed Matter and Materials Physics, 2005, 71(5): 054410
64. Hao J, Hu F, Wang J T, et al. Large enhancement of magnetocaloric and barocaloric effects by hydrostatic pressure in $La(Fe_{0.92}Co_{0.08})_{11.9}Si_{1.1}$ with a $NaZn_{13}$-type structure. Chemistry of Materials, 2020, 32(5): 1807–1818
65. Hao J Z, Hu F X, Yu Z B, et al. The sign of lattice and spin entropy change in the giant magnetocaloric materials with negative lattice expansions. Journal of Magnetism and Magnetic Materials, 2020, 512: 166983
66. Gschneidner K A Jr, Mudryk Y, Pecharsky V K. On the nature of the magnetocaloric effect of the first-order magnetostructural transition. Scripta Materialia, 2012, 67(6): 572–577
67. Pecharsky V K, Gschneidner K A Jr. Tunable magnetic regenerator alloys with a giant magnetocaloric effect for magnetic refrigeration from ~20 to ~290 K. Applied Physics Letters, 1997, 70(24): 3299–3301
68. Pecharsky V K, Pecharsky A O, Gschneidner K A Jr. Uncovering the structure-property relationships in $R_5(Si_xGe_{4-x})$ intermetallic phases. Journal of Alloys and Compounds, 2002, 344(1–2): 362–368
69. Hao J Z, Hu F X, Zhou H B, et al. Large enhancement of magnetocaloric effect driven by hydrostatic pressure in HoCuSi compound. Scripta Materialia, 2020, 186: 84–88
70. Oleś A, Duraj R, Kolenda M, et al. Magnetic properties of DyCuSi and HoCuSi studied by neutron diffraction and magnetic measurements. Journal of Alloys and Compounds, 2004, 363(1−2): 63–67
71. Gong Y Y, Wang D H, Cao Q Q, et al. Electric field control of the magnetocaloric effect. Advanced Materials, 2015, 27(5): 801–805
72. Liu J, Gottschall T, Skokov K P, et al. Giant magnetocaloric effect driven by structural transitions. Nature Materials, 2012, 11(7): 620–626
73. Qiao K, Hu F, Liu Y, et al. Novel reduction of hysteresis loss controlled by strain memory effect in FeRh/PMN-PT heterostructures. Nano Energy, 2019, 59: 285–294
74. Zhang H, Armstrong A, Müllner P. Effects of surface modifications on the fatigue life of unconstrained Ni-Mn-Ga single crystals in a rotating magnetic field. Acta Materialia, 2018, 155: 175–186
75. Mañosa L, Gonzalez-Alonso D, Planes A, et al. Giant solid-state barocaloric effect in the Ni-Mn-In magnetic shape-memory alloy. Nature Materials, 2010, 9(6): 478–481
76. Pecharsky A O, Gschneidner K A Jr, Pecharsky V K. The giant magnetocaloric effect between 190 and 300 K in the $Gd_5Si_xGe_{4-x}$ alloys for $1.4 \leqslant x \leqslant 2.2$. Journal of Magnetism and Magnetic Materials, 2003, 267(1): 60–68
77. Stern-Taulats E, Planes A, Lloveras P, et al. Barocaloric and magnetocaloric effects in $Fe_{49}Rh_{51}$. Physical Review B: Condensed Matter and Materials Physics, 2014, 89(21): 214105
78. Nikitin S A, Myalikgulyev G, Annaorazov M P, et al. Giant elastocaloric effect in FeRh alloy. Physics Letters. [Part A], 1992, 171(3−4): 234–236
79. Biswas A, Chandra S, Phan M H, et al. Magnetocaloric properties of nanocrystalline $LaMnO_3$: Enhancement of refrigerant capacity and relative cooling power. Journal of Alloys and Compounds, 2012, 545: 157–161
80. Qiao K, Wang J, Hu F, et al. Regulation of phase transition and magnetocaloric effect by ferroelectric domains in FeRh/PMN-PT heterojunctions. Acta Materialia, 2020, 191: 51–59
81. Provenzano V, Shapiro A J, Shull R D. Reduction of hysteresis losses in the magnetic refrigerant $Gd_5Ge_2Si_2$ by the addition of iron. Nature, 2004, 429(6994): 853–857
82. Lyubina J, Schäfer R, Martin N, et al. Novel design of $La(Fe,Si)_{13}$ alloys towards high magnetic refrigeration performance. Advanced Materials, 2010, 22(33): 3735–3739
83. Stern-Taulats E, Castan T, Planes A, et al. Giant multicaloric response of bulk $Fe_{49}Rh_{51}$. Physical Review. B, 2017, 95(10): 104424
84. Kübler J, William A R, Sommers C B. Formation and coupling of magnetic moments in Heusler alloys. Physical Review B: Condensed Matter, 1983, 28(4): 1745–1755
85. Sharma V K, Chattopadhyay M K, Roy S B. The effect of external pressure on the magnetocaloric effect of Ni-Mn-In alloy. Journal of Physics Condensed Matter, 2011, 23(36): 366001
86. Liang F X, Hao J Z, Shen F R, et al. Experimental study on coupled caloric effect driven by dual fields in metamagnetic Heusler alloy $Ni_{50}Mn_{35}In_{15}$. APL Materials, 2019, 7(5): 051102
87. Qiao K, Wang J, Zuo S, et al. Enhanced performance of ΔT_{ad} upon frequent alternating magnetic fields in FeRh alloys by introducing second phases. ACS Applied Materials & Interfaces, 2022, 14(16): 18293–18301
88. Aliev A M, Batdalov A B, Khanov L N, et al. Reversible magnetocaloric effect in materials with first order phase transitions in cyclic magnetic fields: $Fe_{48}Rh_{52}$ and $Sm_{0.6}Sr_{0.4}MnO_3$. Applied Physics Letters, 2016, 109(20): 202407
89. Zverev V I, Saletsky A M, Gimaev R R, et al. Influence of structural defects on the magnetocaloric effect in the vicinity of

the first order magnetic transition in $Fe_{50.4}Rh_{49.6}$. Applied Physics Letters, 2016, 108(19): 192405

90. Khaykovich B, Zeldov E, Majer D, et al. Vortex-lattice phase transitions in $Bi_2Sr_2CaCu_2O_8$ crystals with different oxygen stoichiometry. Physical Review Letters, 1996, 76(14): 2555–2558
91. Chang K, Feng W, Chen L Q. Effect of second-phase particle morphology on grain growth kinetics. Acta Materialia, 2009, 57(17): 5229–5236
92. Tang X, Li J, Sepehri-Amin H, et al. Improved coercivity and squareness in bulk hot-deformed Nd-Fe-B magnets by two-step eutectic grain boundary diffusion process. Acta Materialia, 2021, 203: 116479
93. Aliev A M, Batdalov A B, Khanov L N, et al. Magnetocaloric effect in some magnetic materials in alternating magnetic fields up to 22 Hz. Journal of Alloys and Compounds, 2016, 676: 601–605
94. Seo J, McGillicuddy R D, Slavney A H, et al. Colossal barocaloric effects with ultralow hysteresis in two-dimensional metal-halide perovskites. Nature Communications, 2022, 13(1): 2536
95. Li J, Barrio M, Dunstan D J, et al. Colossal reversible barocaloric effects in layered hybrid perovskite $(C_{10}H_{21}NH_3)_2MnCl_4$ under low pressure near room temperature. Advanced Functional Materials, 2021, 31(46): 2105154
96. Aznar A, Lloveras P, Romanini M, et al. Giant barocaloric effects over a wide temperature range in superionic conductor AgI. Nature Communications, 2017, 8(1): 1851